Embedding Calderón Multiplicative Preconditioners in Multilevel Fast Multipole Algorithms

Joris Peeters, Kristof Cools, Ignace Bogaert, Femke Olyslager *Fellow IEEE* and Daniël De Zutter *Fellow IEEE*

Department of Information Technology (INTEC), Ghent University, Sint-Pietersnieuwstraat 41, B-9000 Gent, Belgium, e-mail: Joris.Peeters@intec.ugent.be

Abstract

Calderón preconditioners have recently been demonstrated to be very succesful in stabilising the Electric Field Integral Equation (EFIE) for perfect electric conductors at lower frequencies. Previous authors have shown that, by using a dense matrix preconditioner based on the Calderón identities, the low frequency instability is removed while still maintaining the inherent accuracy of the EFIE. It was also demonstrated that the spectral properties of the Calderón preconditioner are conserved during discretisation if the EFIE operator is discretised with Rao-Wilton-Glisson expansion functions and the preconditioner with Buffa-Christiansen expansion functions. In this article we will show how the Calderón Multiplicative Preconditioner (CMP) can be combined with fast multipole methods to accelerate the numerical solution, leading to an overall complexity of $\mathcal{O}(N \log N)$ for the entire iterative solution. At low frequencies, where the CMP is most useful, the traditional Multilevel Fast Multipole Algorithm (MLFMA) is unstable and we apply the Nondirectional Stable Plane Wave MLFMA (NSPWMLFMA) that resolves the low frequency breakdown of the MLFMA. The combined algorithm will be called the CMP-NSPWMLFMA. Applying the CMP-NSPWMLFMA at open surfaces or very low frequencies leads to certain problems, which will be discussed in this article.

I. Introduction

Integral equations discretised by the Method of Moments (MoM) are very popular for handling scattering problems in the frequency domain as these result in fully error controllable solutions. In this paper we focus on scattering at Perfectly Electrically Conducting (PEC) objects. There exist two independent Boundary Integral Equations (BIE) for this scattering problem, namely the Electric Field Integral Equation (EFIE) and the Magnetic Field Integral Equation (MFIE) [1], which can be linearly combined to form the Combined Field Integral Equation (CFIE). The MFIE is inherently well-posed and as such results in a limited number of iterations when solved iteratively. However, for the same level of discretisation it is significantly less accurate than the EFIE [2], [3]. Regrettably, the EFIE is ill-posed, with the situation becoming worse as the frequency drops (or, a related problem, as the

discretisation becomes finer). We also need to make the distinction between closed and open objects. For the latter ones, the MFIE is not valid and only the EFIE remains viable. In high frequency (HF) simulations of closed objects, both the EFIE and MFIE show spurious solutions at certain resonance frequencies, leading to strongly increased condition numbers (only discretisation error prevents it from becoming infinite). The CFIE is resonance-free but still suffers from a breakdown due to its EFIE contribution, when the mesh-density becomes high. The above outline shows that there are a few situations for which no satisfactory approach is available without the use of efficient preconditioners. Recently [4], [5], a new type of preconditioners has displayed impressive results in stabilising the EFIE at all frequencies, making it an ideal candidate to solve the low frequency (LF) stability problems described above. The preconditioners are based on the Calderón identities, exploiting the fact that the square of the EFIE operator is a second kind operator. Initial formulations [5] of the preconditioner suffered from problems when it was discretised using Rao-Wilton-Glisson (RWG) [6] expansion functions, because the second kind behaviour was lost during the discretisation. This was recently remedied by using Buffa-Christiansen (BC) [7] functions for the preconditioner. With every RWG, a BC is associated on a refined so-called barycentric mesh. Using the RWG-BC combination allows the formulation of the Calderón preconditioner as a matrix multiplication of the MoM matrix with the so-called Calderón Multiplicative Preconditioner (CMP).

Among others, the Multilevel Fast Multipole Algorithm (MLFMA) [8] has been shown to reduce the computational and memory cost in the iterative solution of the MoM system from $\mathcal{O}\left(N^2\right)$ to $\mathcal{O}\left(N \log N\right)$ in the high frequency case. Recently, seamless extensions of the MLFMA to low frequencies have been proposed, such as the Nondirective Stable Plane Wave MLFMA (NSPWMLFMA) [9]. In this paper we will develop a new combined CMP-NSPWMLFMA.

We want to emphasise that the discussion in the remainder of this article is equally applicable to a combination of the CMP with the traditional MLFMA. However, since the MLFMA itself breaks down at low frequencies [8], [9], it is less suitable to combine with Calderón preconditioning that focuses on the low frequency regime. It is also possible to replace the NSPWMLFMA by alternative approaches that are stable at low frequencies, most notably the spectral methods [10] and traditional LF-FMM [8].

This paper is organised as follows. First, in Section II we will briefly revisit the CMP. Section III introduces the NSPWMLFMA and some concepts of fast multipole algorithms that are applied further in the paper. In Section IV, the CMP-NSPWMLFMA is applied to closed surfaces, in both the low and high frequency regime, the latter requiring the linear addition of the MFIE to form the CFIE. Section V demonstrates how to incorporate open PEC objects in the CMP-NSPWMLFMA, while Section VI explains and solves the problems that occur when using the CMP-NSPWMLFMA at extremely low frequencies. Finally, Section VII contains a number of numerical examples that demonstrate the validity and capability of the CMP-NSPWMLFMA combination. In addition, the different sections contain numerical experiments that assert the staked claims therein.

II. Calderón Multiplicative Preconditioner

In frequency domain (an $e^{j\omega t}$ time dependence is assumed and suppressed) the EFIE on a PEC scatterer is defined as

$$-\eta \boldsymbol{T}[\boldsymbol{J}](\boldsymbol{r}) = \boldsymbol{u}_n \times \boldsymbol{E}^i(\boldsymbol{r}), \tag{1}$$

with $\boldsymbol{E}^i$ the incident electric field, $\boldsymbol{J}$ the unknown induced surface current density on the scatterer, ϵ the permittivity, μ the permeability, $\eta = \sqrt{\frac{\mu}{\epsilon}}$ the characteristic impedance and $\boldsymbol{u}_n$ the unit normal on the scatterer surface. The electric-electric operator $\boldsymbol{T}$ is given by

$$\begin{aligned}
\boldsymbol{T}[\boldsymbol{J}](\boldsymbol{r}) &= \frac{1}{\eta}\boldsymbol{u}_n \times \int_S \bar{\mathbf{G}}(\boldsymbol{r}-\boldsymbol{r}') \cdot \boldsymbol{J}(\boldsymbol{r}')\mathrm{d}S' && (2)\\
&= -jk\boldsymbol{u}_n \times \int_S g(|\boldsymbol{r}-\boldsymbol{r}'|)\boldsymbol{J}(\boldsymbol{r}')\mathrm{d}S' + \frac{1}{jk}\boldsymbol{u}_n \times \nabla \int_S \nabla g(|\boldsymbol{r}-\boldsymbol{r}'|) \cdot \boldsymbol{J}(\boldsymbol{r}')\mathrm{d}S' && (3)\\
&= \boldsymbol{T}_s + \boldsymbol{T}_h && (4)
\end{aligned}$$

with $k = \omega\sqrt{\epsilon\mu}$ the wavenumber, $g(\boldsymbol{r}) = \frac{e^{-jk|\boldsymbol{r}|}}{4\pi|\boldsymbol{r}|}$ the homogeneous space scalar Green's function and $\bar{\mathbf{G}}(\boldsymbol{r}) = -j\omega\mu(\bar{\mathbf{I}} + \frac{\nabla\nabla}{k^2})g(|\boldsymbol{r}|)$ the homogeneous space Green's dyadic with $\bar{\mathbf{I}}$ the unit dyadic [11]. The first term $\boldsymbol{T}_s$ represents the contribution from the vector potential, while the second term $\boldsymbol{T}_h$ describes the influence from the scalar potential. The singular value spectrum of this operator has two branches, one going to infinity and one going to zero [12]. As the mesh-density increases, the singular functions associated with these very large and very small singular values can be better resolved and therefore the condition number κ of the resulting impedance matrix in the MoM discretisation will increase. More precisely, $\kappa \sim \frac{1}{(kd)^2}$ with k the wavenumber and d the typical discretisation size. This means that it becomes increasingly difficult to solve the MoM EFIE system iteratively without preconditioning if the mesh-density (unknowns per square wavelength) increases. There exists a wide variety of preconditioners, most directly based on forming approximate inverses of the impedance matrix. The most popular of this kind are block-Jacobi and Incomplete LU (ILU) factorisation [13], which are essentially applicable to any system of linear equations, although their effectiveness may vary significantly. Recent developments include the Approximate MLFMA [14]. Experience shows that this type of preconditioners is generally not performant when dealing with the EFIE at fine mesh-densities although they can be very effective when considering large scatterers requiring not too fine meshes (see also the numerical experiment at the end of this Section). Recently, a new type of preconditioner was proposed, that approaches the problem at the level of the integral equation. It is based on the Calderón identities [15], [12] and preconditions the EFIE by operating $\boldsymbol{T}$ on the EFIE, resulting in a combined operator that is second kind.

One Calderón identity is

$$\boldsymbol{T}^2 = -\frac{1}{4} + \boldsymbol{K}^2 \tag{5}$$

with

$$\boldsymbol{K}[\boldsymbol{J}](\boldsymbol{r}) = -\boldsymbol{u}_n \times \int_S (\nabla \times g(|\boldsymbol{r}-\boldsymbol{r}'|)\bar{\mathbf{I}}) \cdot \boldsymbol{J}(\boldsymbol{r}')\mathrm{d}S' \tag{6}$$

the magnetic-electric operator. The operator $-\frac{1}{4} + \boldsymbol{K}^2$ is second kind and has a bounded spectrum, which means that the integral equation

$$-\eta \boldsymbol{T}^2[\boldsymbol{J}](\boldsymbol{r}) = \boldsymbol{T}[\boldsymbol{u}_n \times \boldsymbol{E}^i(\boldsymbol{r})] \tag{7}$$

is well-posed. When decomposing the $\boldsymbol{T}^2$ operator in contributions from vector and scalar potentials, we arrive at

$$\boldsymbol{T}^2 = \boldsymbol{T}_s^2 + \boldsymbol{T}_s\boldsymbol{T}_h + \boldsymbol{T}_h\boldsymbol{T}_s + \boldsymbol{T}_h^2 \tag{8}$$

The range of $\boldsymbol{T}_h$ is also its kernel, such that $\boldsymbol{T}_h^2 = 0$ [15], [5]. However, when discretising the operators, one must be careful regarding the choice of the expansion functions. When using RWG functions to discretise both the preconditioning $\boldsymbol{T}$ and the EFIE $\boldsymbol{T}$, it appears that the property $\bar{\mathbf{T}}_h \cdot \bar{\mathbf{T}}_h = \bar{\mathbf{0}}$ is not preserved, with $\bar{\mathbf{T}}_h$ the discretised version of $\boldsymbol{T}_h$. A proposed solution is to use the decomposed form (8) and manually omit the $\boldsymbol{T}_h^2$ term. This approach [5] introduces a discretisation error, limiting the accuracy. Recent research [15], [16] has revealed that the use of BC expansion functions for the preconditioning operator and RWG funcions for the EFIE operator maintains the second kind behaviour also after discretisation. This method yields a true Calderón Multiplicative Preconditioner (CMP). While more accurate than the approach using solely RWG functions, it is also faster and more memory efficient because less matrices need to be stored, added and multiplied.

The BC functions are constructed on a refined, so-called barycentric mesh and are div-conforming and quasi curl-conforming. The former property makes them suitable for use as basis functions, the latter assures that the Gram matrix between RWG functions and BC functions is well-conditioned. With every RWG function, a BC function is associated, defined in [7], [15], [16] and illustrated in Fig. 1. Each BC function can be constructed by a weighted sum of 'small' RWG functions on the barycentric mesh. In order to make the BC functions scale identically as their associated RWG function on the original mesh, the BC functions are multiplied by L (see Fig. 1), the sum of the lengths of the two central edges in the barycentric mesh. This will simplify the handling of non-uniform meshes and make the formulation more symmetric.

The following scheme is used to discretise the preconditioned EFIE (similar to [15], but in the frequency domain)

$$\bar{\mathbf{T}}_{BC} \cdot \bar{\mathbf{G}}^{-1} \cdot \bar{\mathbf{T}}_{RWG} \cdot \boldsymbol{X} = \bar{\mathbf{T}}_{BC} \cdot \bar{\mathbf{G}}^{-1} \cdot \langle \boldsymbol{u}_n \times \mathrm{RWG} | \boldsymbol{E}^i \rangle, \tag{9}$$

with $\bar{\mathbf{T}}_{BC} = \langle \boldsymbol{u}_n \times \mathrm{BC} | \boldsymbol{T}(\mathrm{BC}) \rangle$, $\bar{\mathbf{T}}_{RWG} = \langle \boldsymbol{u}_n \times \mathrm{RWG} | \boldsymbol{T}(\mathrm{RWG}) \rangle$ and with the Gram matrix $\bar{\mathbf{G}} = \langle \boldsymbol{u}_\mathrm{n} \times \mathrm{RWG} | \mathrm{BC} \rangle$. The inner product $\langle \mathrm{e}_t | \boldsymbol{D}(\mathrm{e}_b) \rangle$ is defined as the matrix $\bar{\mathbf{D}}$ with $\bar{\mathbf{D}}_{ij} = \int_S \boldsymbol{e}_{t,i}(\boldsymbol{r}) \cdot \int_S \boldsymbol{D}(\boldsymbol{e}_{b,j}(\boldsymbol{r'}))\mathrm{dS'dS}$, with the $\boldsymbol{e}_{t,i}$ a set of test functions and the $\boldsymbol{e}_{b,i}$ a set of basis functions. The inner product $\langle \mathrm{e}_t | \mathrm{e}_b \rangle$ is defined as $\langle \mathrm{e}_t | \boldsymbol{I}(\mathrm{e}_b) \rangle$, with $\boldsymbol{I}$ the identity operator. Finally, the 'right hand side' inner product $\langle \mathrm{e}_t | \boldsymbol{E} \rangle$ is defined as the vector $\boldsymbol{E}$ with $\boldsymbol{E}_i = \int_S \boldsymbol{e}_{t,i}(\boldsymbol{r}) \cdot \boldsymbol{E}(\boldsymbol{r})\mathrm{dS}$. Here, $\boldsymbol{u}_n \times \mathrm{RWG}$ and $\boldsymbol{u}_n \times \mathrm{BC}$ represent the curl-conforming functions obtained by rotating the RWG and BC functions. The Gram matrix is sparse and well-conditioned and its evaluation and multiplication causes barely any additional computational resources.

An example demonstrates the stability properties of the CMP as shown in Fig. 2. The condition number κ_T of $\bar{\mathbf{T}}_{RWG}$ is compared to the condition number κ_{T^2} of $\bar{\mathbf{T}}_{BC} \cdot \bar{\mathbf{G}}^{-1} \cdot \bar{\mathbf{T}}_{RWG}$ over a wide range of mesh sizes. The scattering object is a $1m \times 1m \times 1m$ PEC cube, discretised in triangles of approximate edge size $d = 0.2m$, leading

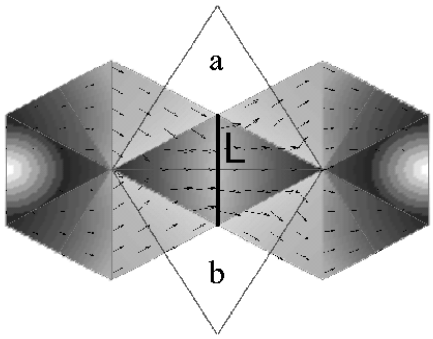

Figure 1. An example BC function. The filling colours (magnitude) and arrows (orientation) illustrate the vectorial behaviour.

Compared to the original definition [7], [15], [16], the BC function is multiplied with a constant factor equal to the length L, i.e. the sum of the lengths of the two central edges of the barycentric mesh. The two large empty triangles (named a and b) indicate the support of the RWG function that is associated with this BC function.

to 450 RWG basis functions. By increasing the wavelength, the mesh-density increases. The non-preconditioned

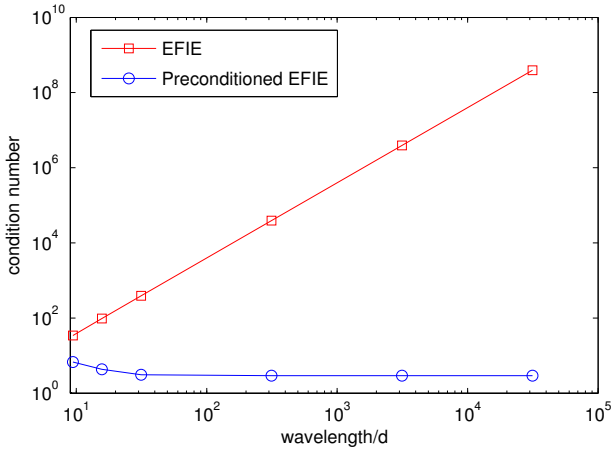

Figure 2. Condition number of the discretised operator for EFIE and Calderón preconditioned EFIE as a function of the inverse mesh size d (in wavelengths)

EFIE has a rapidly rising condition number with increasing mesh-density, while the Calderón preconditioned matrix remains stable.

Some care must be taken when the mesh is non-uniform (to efficiently discretise a large object with important sub-wavelength detail). To guarantee a low condition number κ_G of the Gram matrix, a diagonal preconditioner can be applied that makes all elements on the diagonal equal [16]. A second problem is the condition number of

the entire $\bar{\mathbf{T}}_{BC} \cdot \bar{\mathbf{G}}^{-1} \cdot \bar{\mathbf{T}}_{RWG}$. The diagonal elements must be of the same order of magnutide, which can again be achieved by applying a diagonal preconditioner. Unlike for $\bar{\mathbf{G}}$ the diagonal elements of $\bar{\mathbf{T}}_{BC} \cdot \bar{\mathbf{G}}^{-1} \cdot \bar{\mathbf{T}}_{RWG}$ can not be calculated efficiently, but from (5) and the definition of RWG and BC functions it can be deduced that they scale proportionally to the area of the RWG or its associated BC function. The most general formulation for diagonally preconditioning the entire system is

$$\bar{\mathbf{P}}_L \cdot \bar{\mathbf{T}}_{BC} \cdot \bar{\mathbf{G}}^{-1} \cdot \bar{\mathbf{T}}_{RWG} \cdot \bar{\mathbf{P}}_R \cdot \bar{\mathbf{P}}_R^{-1} \cdot \boldsymbol{X} = \bar{\mathbf{P}}_L \cdot \boldsymbol{B}, \tag{10}$$

which is solved for $\boldsymbol{Y} = \bar{\mathbf{P}}_R^{-1} \cdot \boldsymbol{X}$, after which $\boldsymbol{X}$ follows immediately. In these expressions, $\bar{\mathbf{P}}_L$ and $\bar{\mathbf{P}}_R$ are a left and right preconditioner, respectively. The most balanced system is formed when $\bar{\mathbf{P}}_L$ and $\bar{\mathbf{P}}_R$ are diagonal matrices containing the inverse square root of the areas of the RWG and BC functions, respectively. However, the condition number and iteration count are almost equally low when only a $\bar{\mathbf{P}}_L$ containing the inverse areas of the BC functions or only a $\bar{\mathbf{P}}_R$ containing the inverse areas of the RWG functions is used. Diagonal preconditioners of this kind are very effective when the only source of ill-conditioning is a scaling mismatch, as is the case for both the Gram matrix and $\bar{\mathbf{T}}_{BC} \cdot \bar{\mathbf{G}}^{-1} \cdot \bar{\mathbf{T}}_{RWG}$.

If the object is closed (i.e. it has a finite and nonzero volume) and if it has dimensions about half a wavelength or larger, then the matrix $\bar{\mathbf{T}}^2$ may become singular due to internal resonances. This is typically alleviated by forming the CFIE as a linear combination of the EFIE and the MFIE. The latter one is defined as (the additional cross product with $\boldsymbol{u}_n$ assures that it is well-tested by $\boldsymbol{u}_n \times$ RWG test functions):

$$-\boldsymbol{u}_n \times \{\frac{1}{2} \ - \boldsymbol{K}\}[\boldsymbol{J}](\boldsymbol{r}) = -\boldsymbol{u}_n \times \left[\boldsymbol{u}_n \times \boldsymbol{H}^i(\boldsymbol{r})\right]. \tag{11}$$

Because we have

$$\boldsymbol{T}^2 = -\frac{1}{4} + \boldsymbol{K}^2 = (\boldsymbol{K} - \frac{1}{2})(\boldsymbol{K} + \frac{1}{2}), \tag{12}$$

the operator $\boldsymbol{T}^2$ contains all resonances of the MFIE operator $(\frac{1}{2} - \boldsymbol{K})$ and more. Therefore, forming the Calderón preconditioned CFIE (in the remainder of this article denoted as the Modified CFIE (MCFIE), in accordance with [12]) in the traditional way as

$$\{-\alpha\eta\boldsymbol{T}^2 + (1-\alpha)\eta\boldsymbol{u}_n \times (\frac{1}{2} - \boldsymbol{K})\}(\boldsymbol{J}) = \alpha\boldsymbol{T}(\boldsymbol{u}_n \times \boldsymbol{E}^i) + (1-\alpha)\eta\boldsymbol{u}_n \times [\boldsymbol{u}_n \times \boldsymbol{H}^i], \tag{13}$$

does not lead to a resonance-free integral equation because both terms contain the MFIE resonances. However, the stabilising properties of the Calderón preconditioner are local [12], which allows the use of a localised version $\boldsymbol{T}_L$ of the preconditioner. Unlike $\boldsymbol{T}^2$, $\boldsymbol{T}_L\boldsymbol{T}$ does not contain the MFIE resonances [12].

We will discuss in Section IV how we construct a localised version of the preconditioner, which removes the resonances in the MCFIE. In [17] another localisation technique for the MCFIE is proposed.

Let us now consider the choice of α. In the unpreconditioned CFIE, the number of iterations is minimised around $\alpha \approx 0.2 - 0.3$ [3]. However, the EFIE is more accurate and for a certain tolerance on the RCS it appears that $\alpha \approx 0.5$ obtains the result most efficiently, as a balance between the number of unknowns and the amount of iterations required [18]. In the MCFIE, on the other hand, both the MFIE and locally preconditioned EFIE

contributions are well-conditioned and the number of iterations is almost independent of α. Figure 3 displays the backscattered RCS as a function of α for scattering at a $2m \times 2m$ cube in a high frequency and low frequency case. This illustrates that the typical accuracy considerations still apply. In the low frequency case the number of iterations was always limited to 6 or 7 (for 10^{-6} relative accuracy), while in the high frequency simulation the number of iterations varied from 16 to 8 as α was increased from 0 to 1, regardless of the number of unknowns. The conclusion can be drawn that α should be chosen fairly high, in order to profit from the high accuracy of the EFIE, but not so high as to have a negligble MFIE contribution, which could lead to a strong increase in iterations in case of a resonance. We propose $\alpha \approx 0.8$ as an approximation, but a detailed study (beyond the scope of this article) might reveal an optimal choice. In Section IV we will briefly revisit this topic when an object is simulated at a frequency which displays spurious solutions. A further improvement could include a different expansion scheme for the MFIE (for instance [3]), which enhances its accuracy, to make the choice of α almost completely irrelevant.

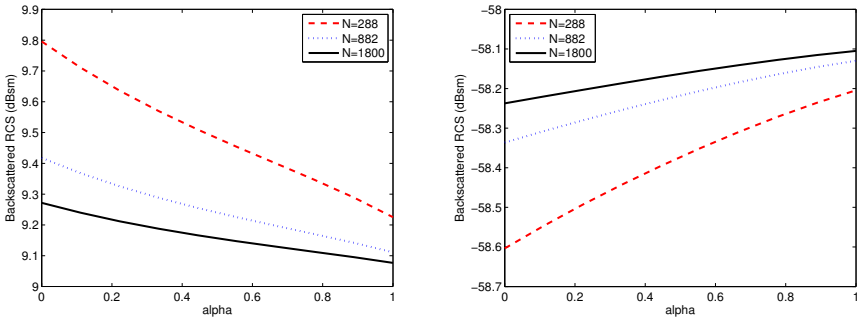

Figure 3. The influence of α in the MCFIE on the backscattered RCS of a $2m \times 2m \times 2m$. The high frequency (left, $f = 4.77e7$ Hz) and low frequency (right, $f = 4.77e5$ Hz) simulations show the value of the backscattered RCS for three different mesh densities, indicated by the number of unknowns N

Of course, the MFIE impedance matrix leads to additional calculation time per iteration and increased memory-usage for storage and, as displayed in Fig. 3, leads to a loss of accuracy. For these reasons, we will only use the MCFIE when the situation requires so, namely for closed objects larger than half a wavelength.

To conclude this section, we compare the Calderón preconditioner with one of the most popular algebraic pre-condioners, the so-called Incomplete LU (ILU) decomposition. ILU preconditioning has been extensively discussed in [13] (and it is beyond the scope of this article to give a detailed overview and comparison). However, as Calderón preconditioning is aimed in particular at stabilising the low frequency (or dense grid) breakdown of EFIE, it is useful to compare both preconditioners in a broadband sense, rather than just the high frequency regime which is most often studied when evaluating algebraic preconditioners. We simulate scattering at a $16m \times 40m$ (open) PEC plate (7568 unknowns), for a range of frequencies, and compare the number of iterations for solution of the EFIE integral equation. The drop tolerance [13] of the ILU preconditioner was chosen for each frequency such that the sparsity of the preconditioner ($\approx 60\%$) is approximately equal to that of the near interaction matrix, from which

it was built. The Calderón preconditioner has 0% sparsity. In this example neither the impedance matrix nor the CMP were accelerated using fast multipole methods, due to its limited size. The results of the comparison (using TF-QMR iterative algorithm [19]) are shown in Table I.

Table I

COMPARISON OF ILU AND CALDERÓN PRECONDITIONER AS A FUNCTION OF THE FREQUENCY (f) AND THE ASSOCIATED ELECTRIC DISCRETISATION SIZE $\frac{d}{\lambda}$. THE ITERATION COUNT IS SHOWN FOR A SOLUTION TO RELATIVE ACCURACY 10^{-6} FOR THE UNPRECONDITIONED CASE ('NONE') AND USAGE OF THE ILU AND CALDERÓN ('CAL') PRECONDITIONER, FOR SCATTERING AT A PEC PLATE.

f (Hz)	$\frac{d}{\lambda}$	$N_{it,none}$	$N_{it,ILU}$	$N_{it,Cal}$
$4.77 \cdot 10^7$	$8 \cdot 10^{-2}$	577	5	51
$1.59 \cdot 10^7$	$2.6 \cdot 10^{-2}$	748	8	33
$4.77 \cdot 10^6$	$8 \cdot 10^{-3}$	669	52	17
$1.59 \cdot 10^6$	$2.6 \cdot 10^{-3}$	889	198	15
$4.77 \cdot 10^5$	$8 \cdot 10^{-4}$	915	> 1000	15

It is clear that the ILU preconditioner performs well at high frequencies (discretisation approximately $\frac{\lambda}{10}$), as was already shown by previous authors [13], but quickly breaks down when the frequency drops (or the grid density increases), while the Calderón preconditioner is less effective at high frequencies but is very stable at low frequencies. The low frequency breakdown of ILU is in accordance with an observation made later in this article, namely that the sparsity of the preconditioner must decrease when the frequency goes down, in order to remain effective. The Calderón approach leads to a fully dense matrix and as such does not suffer from this effect. Because of this, it is however more computationally expensive (although, as will be shown, this is not prohibitive to the complexity after applying fast multipole methods). As such, at high frequencies the algebraic preconditioners are at least competitive with and probably preferable to Calderón techniques and the focus in the remainder of the article will be predominantly on the performance in a broadband frequency range.

III. NON-DIRECTIONAL STABLE PLANE WAVE MULTI-LEVEL FAST MULTIPOLE ALGORITHM

The MLFMA [8] is based on a propagating plane wave decomposition of the Green's function,

$$\frac{e^{-jkr_{ji}}}{4\pi r_{ji}} \approx \int e^{-j\boldsymbol{k}\cdot\boldsymbol{r}_{jm}} T_{mm'}(\boldsymbol{k}, \boldsymbol{r}_{mm'}) e^{j\boldsymbol{k}\cdot\boldsymbol{r}_{im'}} \mathrm{d}\hat{k} \tag{14}$$

with

$$T_{mm}(\boldsymbol{k}, \boldsymbol{r}_{mm'}) = \frac{-jk}{(4\pi)^2} \sum_{l=0}^{L} (-j)^l (2l+1) h_l^{(2)}(kr_{mm'}) P_l(\hat{r}_{mm'} \cdot \hat{k}) \tag{15}$$

with $h_l^{(2)}$ the second kind spherical Hankel function of order l, P_l the Legendre polynomial of degree l and the vectors $\boldsymbol{r}_{jm}$, $\boldsymbol{r}_{mm'}$ and $\boldsymbol{r}_{im'}$ illustrated on Fig. 4.

All basis and test functions are divided into localised box-shaped groups. Using (14), a matrix-vector product can be executed as follows: all basis functions (multiplied by their expansion coefficient) in a group can be aggregated into an outgoing radiation pattern, which is then translated to an incoming radiation pattern at the receiving group.

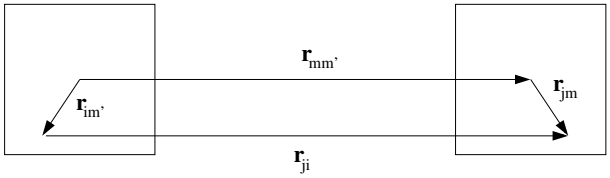

Figure 4. The vectors required for aggregation, translation and disaggregation.

The incoming radiation pattern is then disaggregated to the test functions, completing the interaction between those two groups. The addition theorem is only valid when the largest possible sum of the aggregation and disaggregation distance is smaller than the distance of translation, requiring at least one box seperation between groups that interact through MLFMA. However, in practice, the MLFMA scheme can only be used for boxes that are separated by at least n_t boxes, with $n_t \geq 1$ and defined by the desired accuracy and the box size at the lowest level [8], [9]. In practical simulations, n_t typically lies between 1 and 3. Interactions between expansion functions of boxes that are closer to each other are not accelerated with the MLFMA scheme and need to be calculated by direct evaluation of the Green's function. The radiation patterns are sampled in the quadrature points used for the integration in (14). The number of plane waves required for an accurate integration depends on the group size. When using a multi-level scheme, where nearby groups are hierarchically assembled into larger groups, some form of interpolation and anterpolation is required between the levels. In [8], uniform sampling in the ϕ coordinate and Gauss-Legendre sampling in the θ coordinate is used, while aggregating to a higher level relies on local Langrange interpolation. An alternative approach [20] suggests the use of uniform sampling for both coordinates, allowing for Fast Fourier Transform (FFT) interpolation and anterpolation, which is global and more accurate. In the next sections, we will opt for the latter method.

The MLFMA suffers from the so-called low frequency (LF) breakdown [9], which is caused by a numerical instability rooted in the supra-exponential behaviour of the Hankel function when the order becomes larger than its argument. The higher order terms, even though they should largely cancel out after integration, swamp the dominant lower order terms which are lost then in the process. When the electric translation distance drops, the argument of the Hankel function decreases and the instability becomes more prominent. In practice, the MLFMA cannot obtain a reasonable accuracy for boxes below a quarter of a wavelength. This is especially relevant to this paper because we are looking at Calderón preconditioning techniques for fine meshes.

Recently, research for alternatives that are stable over a wide frequency range has resulted into a number of efficient algorithms. A first one is based on a spectral decomposition [10] of the Green's function and includes evanescent waves in addition to the propagating waves. Because the formulation is only valid in one half-space, it requires multiple radiation patterns. Nevertheless, very efficient interpolation routines have been developed, making this method suitable for broadband simulations. Another approach, the Nondirective Stable Plane Wave Multi-Level Fast Multipole Algorithm (NSPWMLFMA) [9], is closely related to the MLFMA and stabilises the plane wave

decomposition for all frequencies. By shifting the θ coordinate into the complex plane over a certain distance χ, the terms in the translation operator sum are normalised. However, this scheme only works for z-directed translations. Translations in other directions can be treated by a rotation, aligning them with the z-axis. To avoid a different radiation pattern for every direction of translation, a basis of plane waves is constructed through a QR-procedure that contains enough information for all the different orientations. The rotation and transformation to uniform points can be included in the translation operator, which keeps its diagonal property. The result is a scheme that is very similar to the MLFMA, the only drawback being that the interpolations can no longer be efficiently treated with the FFT algorithm but now require a dense matrix. This drawback limits the scheme to the low frequency region, where L is approximately independent of the electric box size. However, the entire method still becomes broadband by switching to the MLFMA as soon as the boxes become large enough. This can be done seamlessly by setting $\chi = 0$ and using the uniform sample points and FFT interpolation from a certain level. Compared to the spectral methods, the NSPWMLFMA requires aggregation of only one radiation pattern, but has less efficient interpolations between the levels. In all simulations and tests, we will opt for the NSPWMLFMA, but it needs to be stressed that all techniques discussed further are essentially independent of the specific algorithm used.

The remainder of this section is devoted to introducing and clarifying a few subtle aspects of the MLFMA that are important to Calderón preconditioning. First of all, we will generally use the vectorial formulation, based on the dyadic representation in (2). The Green's dyadic can be decomposed as

$$\bar{\mathbf{G}}(\boldsymbol{r}_{ji}) \approx \int (\bar{\mathbf{I}} - \hat{k}\hat{k}) e^{-j\boldsymbol{k}\cdot\boldsymbol{r}_{jm}} T_{mm'}(\boldsymbol{k}, \boldsymbol{r}_{mm'}) e^{j\boldsymbol{k}\cdot\boldsymbol{r}_{im'}} \,\mathrm{d}\hat{k} \tag{16}$$

Because $\bar{\mathbf{I}} - \hat{k}\hat{k} = \hat{\theta}\hat{\theta} + \hat{\phi}\hat{\phi}$ and because it is a projection operator, the radiation patterns are fully determined with only two independent components, namely a θ and ϕ component (as one could expect from a far field pattern). The scalar formulation of the MLFMA relies on (3) and uses four components (three Carthesian components for the vector potential and one for the scalar potential). The number of components can be reduced to three by exploiting the Lorenz gauge, but it is still less efficient than the vectorial formulation which we will use in the next section. An important aspect of vectorial formulations is the choice of the truncation limit L. A number of implicit and explicit expressions for L exist for the scalar case [21], [8]. In the HF regime it can be shown [8] that the vectorial case requires two extra terms to be included for the EFIE, to compensate for the $\nabla\nabla\cdot$ operation in the Green's dyadic. However, an expression valid over the entire frequency range is significantly more analytically involved. The MFIE contains only one ∇ operation and as such it is expected to require a lower L than the EFIE. A detailed study is conducted in [21] and we will limit ourselves here to Fig. 5, displaying the required L for the scalar case, the MFIE and the EFIE, to approximate respectively the Green's function $g(\boldsymbol{r})$, the electric-electric Green's dyadic $\bar{\mathbf{G}}(\boldsymbol{r})$ and the electric-magnetic Green's dyadic $\nabla \times g(\boldsymbol{r})\bar{\mathbf{I}}$ with 10^{-3} accuracy and $n_t = 3$.

As expected, in the HF-regime (i.e. for boxes that are of the order of a wavelength or larger) the differences are small and the Green's dyadics require at most one or two extra terms, compared to the scalar Green's function. However, in the LF regime the differences are much more pronounced and are rooted in the differential operators that occur in the Green's dyadics. For the purpose of this article, we observe that at lower frequencies the MFIE

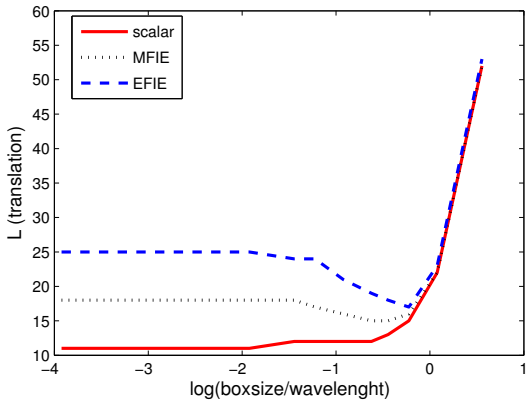

Figure 5. Truncation L required for approximating within a tolerance of 10^{-3} the Green's function (denoted 'scalar'), the electric-electric Green's dyadic (denoted 'EFIE') and the magnetic-electric Green's dyadic (denoted 'MFIE'), as a function of box size for $n_t = 3$.

requires significantly less terms in the series than the EFIE for the same accuracy.

The previously mentioned L denotes the number of terms in the translation operator. The required sampling rate for the Ewald sphere integration (in the case of NSPWMLFMA) can be shown to be $(L+1)^2$. However, this is not the number of sample points required to store the aggregation or disaggregation patterns with sufficient accuracy. One can use a smaller amount of sample points, namely $(L'+1)^2$, expressed by means of a parameter L' (with $L' \leq L$). L' is defined as the smallest number for which $(L'+1)^2$ sample points at the aggregation and disaggregation stages still lead to the desired accuracy after interpolation to and anterpolation from $(L+1)^2$ sample points at the translation stage. This is particularly useful at the lowest level, where aggregation and disaggregation are done through dense matrices that need to be stored. In the high frequency limit one expects L' to approximate $\frac{L}{2}$, which would mean a fourfold reduction in memory. A detailed analysis is given in [21], in this article we will restrict ourselves to Fig. 6, showing the required L' for accurate aggregation and disaggregation.

While using $L' < L$ significantly saves memory, it will increase computational cost due to the extra interpolations and anterpolations required. If the number of iterations is limited, e.g. by using a Calderón preconditioner, such that the overall run-time is dominated by setup, then the reduced memory-usage can be more important than the increased computational iteration cost.

In the next three sections, we will demonstrate how the NSPWMLFMA (or, for high frequencies, the MLFMA alone) can be efficiently used to accelerate the Calderón preconditioned EFIE. We will start with the most straightforward case: that of closed objects.

IV. Closed Objects

Storage and calculation of (9) is of $\mathcal{O}\left(N^2\right)$ complexity due to the dense matrices $\bar{\mathbf{T}}_{BC}$ and $\bar{\mathbf{T}}_{RWG}$. Both these complexities can be reduced to $\mathcal{O}\left(N \log N\right)$ by applying the NSPWMLFMA (including the transition to MLFMA when the boxes become large), which makes the scheme useful for objects requiring many unknowns.

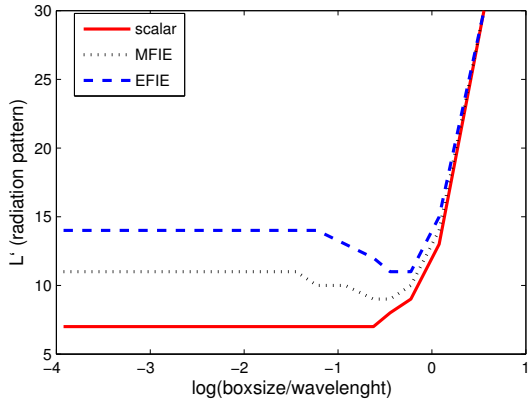

Figure 6. Aggregation L' required such that after interpolation to L the Green's function ('scalar'), the electric-electric Green's dyadic ('EFIE') and the magnetic-electric Green's dyadic ('MFIE') can still be approximated within a tolerance of 10^{-3}, as a function of box size for $n_t = 3$.

Application of fast methods to the impedance matrix $\bar{\mathbf{T}}_{RWG}$ has been studied extensively before and has been shown to be highly effective. The oct-tree used for the RWG functions can be re-used for the BC functions. Since every BC function is associated with one RWG function and has approximately the same centroid and spatial extent, the BC function can be assigned to the same box as the corresponding RWG function. This makes extension of existing codes significantly easier. Let us first look at the simulation of (closed) objects below their first resonance frequency, in which case the EFIE alone is sufficient to obtain an accurate solution. As an example, a $2\mathrm{m} \times 2\mathrm{m} \times 2\mathrm{m}$ cube is considered, illuminated by a plane wave with frequency $4.77 \cdot 10^7$ Hz, which is well below the first resonance frequency. Table II shows the number of iterations (N_{it}), the time per iteration (T_{it}) and the memory for aggregation/disaggregation matrices (M_{agg}), near interactions (M_{near}) and translation operators (M_{trans}) as a function of the number of unknowns (N) and mesh-density (ρ_m as number of unknowns per square wavelength). Additionally, the memory is indicated that would be required for a classical MoM simulation without use of fast multipole techniques (M_{class}). The relative accuracy of the iterative solution is 10^{-3}. The Transpose Free Quasi Minimal Residual (TFQMR) iterative algorithm [19] was used in this and all later examples.

Table II

STATISTICS FOR SCATTERING SIMULATIONS OF A $2\mathrm{m} \times 2\mathrm{m} \times 2\mathrm{m}$ CUBE AT $4.77 \cdot 10^7$ HZ AS A FUNCTION OF THE NUMBER OF UNKNOWNS (N) AND MESH-DENSITY (ρ_m AS NUMBER OF UNKNOWNS PER SQUARE WAVELENGTH).

N	ρ_m	N_{it}	T_{it} (s)	M_{near} (MByte)	M_{agg} (MByte)	M_{trans} (MByte)	M_{class} (MByte)
288	$4.74 \cdot 10^2$	5	0.026	2.53	0	0	2.53
1152	$1.90 \cdot 10^3$	6	0.118	40.5	0	0	40.5
4608	$7.58 \cdot 10^3$	6	1.36	200	225	7.4	648
18432	$3.03 \cdot 10^4$	6	20.7	684	992	24	$1.04 \cdot 10^4$
73728	$1.22 \cdot 10^5$	6	137	2348	3876	41	$1.66 \cdot 10^5$
294 912	$4.85 \cdot 10^5$	6	664	8691	15876	113	$2.66 \cdot 10^6$

The table shows that, even for very high mesh-densities, the scheme including NSPWMLFMA maintains the LF stability of the integral equation. Also note that the electrical size of the cube is approximately 0.3λ, which coincides more or less with the lowest level box size of the traditional (high frequency) MLFMA. For stability reasons (see Section III), this box size can not be reduced in the MLFMA and therefore it can not be applied in this example. This illustrates the importance of having an LF stable fast multipole technique (like the NSPWMLFMA) in combination with the CMP.

When the frequency is high such that resonance solutions cannot be excluded, the MCFIE (13) is needed. When not using a Calderón preconditioner, the impedance matrices resulting from the EFIE and MFIE can simply be added at setup-time, resulting in no additional memory or CPU time during the iterative process. However, in our scheme this is no longer possible, because $\bar{\mathbf{T}}_{BC}\cdot\bar{\mathbf{G}}^{-1}$ must be applied to $\bar{\mathbf{T}}_{RWG}\cdot\boldsymbol{J}$ alone. Therefore, the memory required for the near interactions of the MFIE must be stored seperately. However, the distant interactions can be stored efficiently since the aggregations and translations of $\bar{\mathbf{K}}_{RWG}$ and $\bar{\mathbf{T}}_{RWG}$ are identical, with $\bar{\mathbf{K}}_{RWG} = \langle \boldsymbol{u}_n \times \mathrm{RWG} | \boldsymbol{K}(\mathrm{RWG}) \rangle$. The sharing of aggregations and translations can also be exploited during the iterative process, by treating MFIE and EFIE together for aggregation and translation and only seperating them for disaggregation.

The sampling rate for the radiation patterns of the MFIE is significantly smaller than that of the EFIE, such that the disaggregation matrices of the MFIE can be stored more compactly than those of the EFIE. We have previously indicated that $\boldsymbol{T}^2$ contains all the resonances of $\frac{1}{2} - \boldsymbol{K}$ and more, such that we must use a localised version of $\bar{\mathbf{T}}_{BC}$ (denoted as $\bar{\mathbf{T}}_{L,BC}$) in order to obtain a truly resonance-free equation. A number of methods exist to create a $\bar{\mathbf{T}}_{L,BC}$, but here we will opt to omit interactions over a distance longer than 1λ. Omitting distant interactions beyond a certain translation distance has the secondary advantage of saving some memory and accelerating the matrix-vector product, even though these gains are generally marginal because most computational effort is done on the lowest levels, i.e. at short distances. This implies that when the frequency goes down (and the mesh remains identical), $\bar{\mathbf{T}}_{L,BC}$ becomes less sparse, eventually being fully dense when the scatterer is smaller than the wavelength. An alternative method for localisation (using jk instead of k in $\bar{\mathbf{T}}_{L,BC}$ [17]) shows essentially the same behaviour. Although a detailed study is beyond the scope of this article, this behaviour could indicate why the (sparse) algebraic preconditioners break down when the frequency drops. Although in general high frequency simulations can be treated efficiently with algebraic preconditioners like ILU, using a Calderón preconditioner for electrically large objects can be necessary when the mesh-density is high (for instance, due to fine geometrical features), leading to a high condition number due to the EFIE contribution in the unpreconditioned CFIE.

In the following example we consider a $2\lambda \times 2\lambda \times 2\lambda$ resonating cube with a locally refined mesh near the edges, to more accurately catch the singular behaviour of the induced currents. The object has dimensions larger than half a wavelength, requiring CFIE or MCFIE. For a fair comparison between the two solution methods it is necessary to solve the solution vectors for the same accuracy. During the iterative process, when solving the system $\bar{\mathbf{A}}\cdot\boldsymbol{X} = \boldsymbol{B}$, the stopping criterium is such that $\frac{||\bar{\mathbf{A}}\cdot\boldsymbol{X}-\boldsymbol{B}||}{||\boldsymbol{B}||} < \epsilon$. When using a preconditioner $\bar{\mathbf{M}}$, the stopping criterium used is $\frac{||\bar{\mathbf{M}}\cdot(\bar{\mathbf{A}}\cdot\boldsymbol{X}-\boldsymbol{B})||}{||\bar{\mathbf{M}}\cdot\boldsymbol{B}||} < \epsilon$. However, these do not lead to solutions that are equally accurate, because of the difference

in condition number of $\bar{\mathbf{A}}$ and $\bar{\mathbf{M}} \cdot \bar{\mathbf{A}}$. We will use the *a posteriori* stopping criterium of $\frac{\boldsymbol{X}-\boldsymbol{X}_e}{\boldsymbol{X}_e} < \epsilon$, with $\boldsymbol{X}_e$ an approximation of the exact solution that we obtained by first solving for a few additional orders of magnitude accuracy. While this has no practical purposes, because the exact solution is not known at run-time, it allows for a more accurate and fair assessment of preconditioners. A significant increase in iteration count is observed for those where $\bar{\mathbf{M}} \cdot \bar{\mathbf{A}}$ (or just $\bar{\mathbf{A}}$ is no preconditioner is applied) is ill-conditioned.

The results are displayed in Table III, for $\epsilon = 10^{-6}$. The numerical value after CFIE and MCFIE indicates the coefficient α. Note that both the EFIE and the MFIE have spurious solutions. However, only those of the MFIE will effectively radiate, leading to incorrect radar cross sections. The EFIE will lead to incorrect current densities but results in the correct field values. Hence, even though the MFIE (its exact solution $\boldsymbol{X}_e$ is finite, due to the discretisation, so the iteration count can be determined) is included in Table III for the sake of completeness, it cannot be considered a dependable solution method in the high frequency region. This is illustrated in Fig. 7, displaying the radar cross section of the cube at large distance, obtained using most of the integral equations from Table III.

Table III

COMPARISON OF THE VARIOUS INTEGRAL EQUATIONS FOR THE SOLUTION OF A RESONATING CUBE ($N = 150\,390$).

Equation	Operator	N_{it}	T_{it} (s)
EFIE	$\boldsymbol{T}$	≈ 50000	161
MFIE	$\boldsymbol{K}$	136	161
$\text{CFIE}_{0.2}$	$0.2\boldsymbol{T} + 0.8\eta\boldsymbol{K}$	109	161
$\text{MCFIE}_{0.05}$	$0.05\boldsymbol{T}_L \cdot \boldsymbol{T} + 0.95\eta\boldsymbol{K}$	64	473
$\text{MCFIE}_{0.5}$	$0.5\boldsymbol{T}_L \cdot \boldsymbol{T} + 0.5\eta\boldsymbol{K}$	15	473
$\text{MCFIE}_{0.8}$	$0.8\boldsymbol{T}_L \cdot \boldsymbol{T} + 0.2\eta\boldsymbol{K}$	13	473
$\text{MCFIE}_{0.95}$	$0.95\boldsymbol{T}_L \cdot \boldsymbol{T} + 0.05\eta\boldsymbol{K}$	23	473

The accuracy of the CFIE and MCFIE are good and, as expected, depend on the choice of α (a high α means the accurate EFIE dominates the slightly more inaccurate MFIE, as previously discussed). Table III explains our earlier recommendation of $\alpha \approx 0.8$ in the MCFIE: the accuracy is high and the number of iterations is low. The MFIE alone leads to a completely incorrect far field, as a result of the radiating spurious mode.

It is obvious that NSPWMLFMA-accelerated Calderón preconditioners have significant value in situations where the mesh-density is too high for the EFIE to converge fast. The additional cost per iteration is more than compensated for by the highly reduced number of iterations. The improved spectral properties guarantee robustness.

V. OPEN SURFACES

One of the most powerful features of BC functions is that $\bar{\mathbf{T}}_{BC}$ effectively preconditions $\bar{\mathbf{T}}_{RWG}$ even in the case of open structures [16], something hitherto impossible using only RWG functions. As shown in [12], on open surfaces we solve for $\boldsymbol{J} = \boldsymbol{J}_+ + \boldsymbol{J}_-$ as the sum of the current densities on both sides of the surface, using the

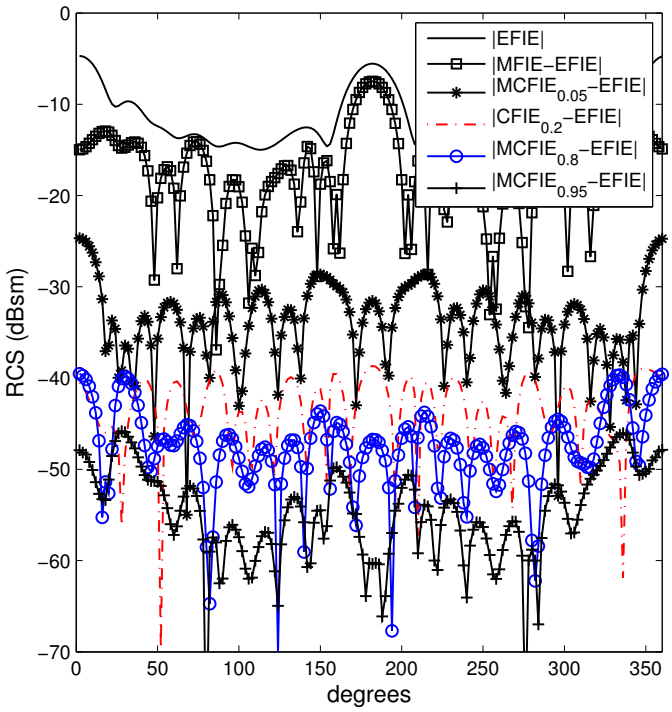

Figure 7. Comparison of the radar cross section, using various integral equations (see also Table III). The absolute difference of the results using MFIE, CFIE and MCFIE with the EFIE (used as a reference) are plotted along a large circle around the cubic scattering object. For convenience, the entries in the legend are ordered by descending value along the 180° direction.

EFIE

$$-\eta \boldsymbol{T}_{++}[\boldsymbol{J}](\boldsymbol{r}) = \boldsymbol{u}_n \times \boldsymbol{E}^i(\boldsymbol{r}) \tag{17}$$

However, contrary to closed surfaces, $\boldsymbol{T}_{++}$ cannot be linked to $\boldsymbol{K}_{++}$, such that $\boldsymbol{T}_{++}^2$ cannot be shown to be a well-posed operator. Some arguments indicating the superiority of $\boldsymbol{T}_{++}^2$ over $\boldsymbol{T}_{++}$ are given in [12]. Still, through a Helmholtz-decomposition it can be shown that the range of $\bar{\mathbf{T}}_{h++,RWG}$ is the kernel of $\bar{\mathbf{T}}_{h++,BC}$ [15]. In the remainder of this section, $\bar{\mathbf{T}}_{++}$ will simply be denoted as $\bar{\mathbf{T}}$. Due to the particular construction of the BC functions at the edges, the scheme described by (9) applies to open structures as well. However, application of the vectorial NSPWMLFMA to $\bar{\mathbf{T}}_{BC}$ faces some difficulties due to the fact that BC functions, contrary to RWG functions, have a component normal to the edge. In order to be able to calculate the near interactions for the contribution due to the scalar potential, the integral

$$\int_{S_i} \boldsymbol{b}_i(\boldsymbol{r}) \cdot \nabla \int_{S_j} \nabla g(|\boldsymbol{r} - \boldsymbol{r}'|) \cdot \boldsymbol{b}_j(\boldsymbol{r}') \mathrm{d}S' \mathrm{d}S \tag{18}$$

must be calculated. When $\boldsymbol{b}$ does not have a component normal to the edge, this can be reduced to the less singular form

$$-\int_{S_i} \nabla \cdot \boldsymbol{b}_i(\boldsymbol{r}) \int_{S_j} g(|\boldsymbol{r}-\boldsymbol{r}'|) \nabla \cdot \boldsymbol{b}_j(\boldsymbol{r}') \mathrm{d}S' \mathrm{d}S \tag{19}$$

of which the singular part of the inner integration can be integrated analytically for linear functions $\boldsymbol{b}$ [22]. However, in the case of BC functions, the normal component gives rise to equivalent line charges. These line charges lead to non-integrable integrals over the edge. While this may seem an unsurmountable issue, in previous publications [15] these line charges were simply omitted. Practice shows that it leads to the desired results. In the NSPWMLFMA the omission of the line charges requires a different formulation for the distant interactions. The vectorial formulation, based on the decomposition of the Green's dyadic, does not move a ∇ to the basis and test functions and thus includes the contribution of the line charges. This would lead to a mixed matrix, where the near interactions omit the line charges and the far interactions include them, jeopardising the preconditioning effect. For consistency, the scalar formulation is required, using four scalar radiation patterns. The extra computational cost is relatively limited. There is no modification to the storage of $\bar{\mathbf{T}}_{RWG}$, nor to the calculation of $\bar{\mathbf{T}}_{RWG} \cdot \boldsymbol{J}$. The near interactions of $\bar{\mathbf{T}}_{BC}$ are treated identically as for closed objects. Only the distant interactions related to $\bar{\mathbf{T}}_{BC}$ require twice as much memory and computational time, due to a doubling of the number of the radiation pattern components. As an illustration, the simulation of a $2m \times 2m$ plate is considered, at a frequency of $4.77 \cdot 10^7$, for varying mesh-density. The results are displayed in Table IV and show the number of iterations (N_{it}), the time per iteration (T_{it}) and the memory for aggregation/disaggregation matrices (M_{agg}), near interactions (M_{near}) and translation operators (M_{trans}) as a function of the number of unknowns (N) and mesh-density (ρ_m as number of unknowns per square wavelength). Additionally, the memory is indicated that would be required for a classical MoM simulation without use of fast multipole techniques (M_{class}). The relative accuracy of the iterative solution is 10^{-3}.

Table IV

STATISTICS FOR SCATTERING SIMULATIONS OF A 2m $\times$ 2m PLATE AT $4.77 \cdot 10^7$ HZ AS A FUNCTION OF THE NUMBER OF UNKNOWNS (N) AND MESH-DENSITY (ρ_m AS NUMBER OF UNKNOWNS PER SQUARE WAVELENGTH).

N	ρ_m	N_{it}	T_{it} (s)	M_{agg} (MByte)	M_{near} (MByte)	M_{trans} (MByte)	M_{class} (MByte)
12160	$1.2 \cdot 10^5$	8	33	981	291	3.8	$4.5 \cdot 10^3$
48896	$4.8 \cdot 10^5$	8	145	3774	1250	5	$8 \cdot 10^4$
196096	$1.9 \cdot 10^6$	8	606	15465	5054	7	$1.2 \cdot 10^5$

The results indicate that the preconditioner has the same effect on open surfaces as it has on closed ones. While in general the condition number of $\bar{\mathbf{T}}_{BC} \cdot \bar{\mathbf{G}}^{-1} \cdot \bar{\mathbf{T}}_{RWG}$ for open surfaces is slightly higher than that for closed surfaces, the same independence of mesh-density is observed. The previous example demonstrates the LF behaviour. The Calderón preconditioner can also be applied to HF simulations (characterised by mesh-sizes of the order 0.1λ). In Table V the number of iterations is compared when using the unpreconditioned matrix $\bar{\mathbf{T}}_{RWG}$, the full $\bar{\mathbf{T}}_{BC} \cdot \bar{\mathbf{G}}^{-1} \cdot \bar{\mathbf{T}}_{RWG}$ matrix and a local preconditioner as in $\bar{\mathbf{T}}_{L,BC} \cdot \bar{\mathbf{G}}^{-1} \cdot \bar{\mathbf{T}}_{RWG}$. The dimensions of the plate

are systematically increased, while the frequency remains at $4.77 \cdot 10^7$ Hz. The relative accuracy of the iterative solution is 10^{-3}.

Table V

COMPARISON OF THE ITERATION COUNT N_{it} AND MEMORY USAGE M (IN MB) FOR A HF SCATTERING SIMULATION AT A SQUARE PLATE OF INCREASING SIZE (N UNKNOWNS) FOR MATRICES $\bar{\mathbf{T}}_{RWG}$ (DENOTED $\bar{\mathbf{T}}$), $\bar{\mathbf{T}}_{BC} \cdot \bar{\mathbf{G}}^{-1} \cdot \bar{\mathbf{T}}_{RWG}$ (DENOTED $\bar{\mathbf{T}}^2$) AND $\bar{\mathbf{T}}_{L,BC} \cdot \bar{\mathbf{G}}^{-1} \cdot \bar{\mathbf{T}}_{RWG}$ (DENOTED $\bar{\mathbf{T}}_L\bar{\mathbf{T}}$).

Size (m^2)	N	$N_{it}(\bar{\mathbf{T}})$	$N_{it}(\bar{\mathbf{T}}^2)$	$N_{it}(\bar{\mathbf{T}}_L\bar{\mathbf{T}})$	$M(\bar{\mathbf{T}})$	$M(\bar{\mathbf{T}}^2)$	$M(\bar{\mathbf{T}}_L\bar{\mathbf{T}})$
16×16	3008	178	28	19	138	350	350
20×20	4720	226	34	13	228	573	573
24×24	6816	220	43	13	338	845	845
28×28	9296	304	49	13	473	1177	1177
32×32	12160	322	55	13	629	1559	1558
36×36	15408	310	67	13	807	1995	1994
40×40	19040	382	73	13	1010	2491	2490
44×44	23056	448	82	13	1230	3030	3028
60×60	42960	592	112	15	2293	5626	5623
80×80	76480	700	180	17	4144	10138	10135
120×120	172480	>1000	316	20	9475	23120	23116
160×160	306560	>1000	>1000	24	16983	41386	41380

As expected, the number of iterations for the unpreconditioned EFIE increases rapidly. More surprising, however, is the fact that the iteration count for $\bar{\mathbf{T}}_{BC} \cdot \bar{\mathbf{G}}^{-1} \cdot \bar{\mathbf{T}}_{RWG}$ rises relatively fast as well (even though it remains considerably lower than the EFIE alone), while $\bar{\mathbf{T}}_{L,BC} \cdot \bar{\mathbf{G}}^{-1} \cdot \bar{\mathbf{T}}_{RWG}$ seems to keep things under control. In order to get a better understanding of this phenomenon, the eigenvalue spectra for both are displayed in Fig. 8 for the $20m \times 20m$ plate.

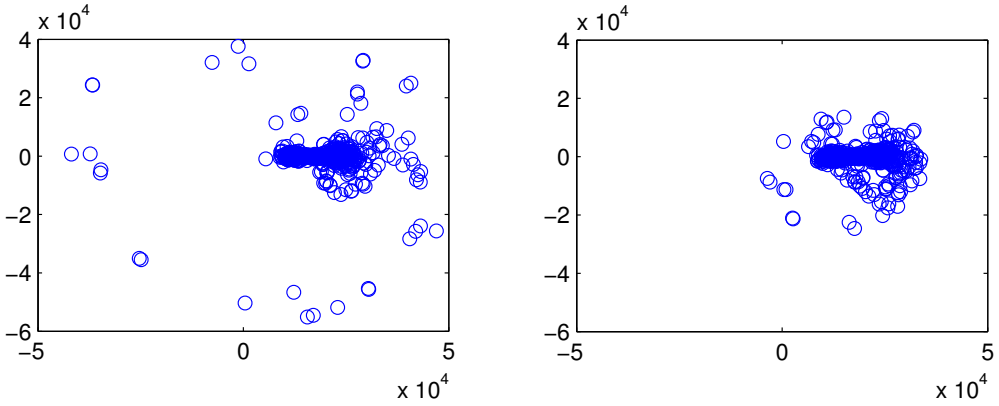

Figure 8. Eigenvalue spectra (in the complex plane) of the matrices $\bar{\mathbf{T}}_{BC} \cdot \bar{\mathbf{G}}^{-1} \cdot \bar{\mathbf{T}}_{RWG}$ (left) and $\bar{\mathbf{T}}_{L,BC} \cdot \bar{\mathbf{G}}^{-1} \cdot \bar{\mathbf{T}}_{RWG}$ (right) for a square plate

Unlike for closed objects, the global operator $\boldsymbol{T}^2$ can not be analytically related to a second-kind operator [12] and

displays eigenvalues in all quadrants of the complex plane. In addition to a slightly increased condition number, this scattering of the eigenvalues causes difficulties for iterative solvers, which perform optimally when the eigenvalues are clustered and restricted to certain areas of the complex plane [23]. When using the local preconditioner, the scattering is limited and as a consequence the solution is found in less iterations. In general, it is better to use a local preconditioner, not just as a way to save resources but also to obtain faster convergence. A detailed study of why the local preconditioner reduces the scattering is beyond the scope of this article. It is, however, related to the fact that, using a local instead of global preconditioner, the influence from the edges on the rest of the surface is reduced. This explains why open structures with a high edge to surface ratio (for instance Split Ring Resonators) still cause compactness issues, even when using a local preconditioner. The memory comparison in Table V shows that for open surfaces the scheme with a preconditioner requires about 2.5 times the memory of the unpreconditioned scheme. This is due to the previously discussed fact that the scalar formulation of (NSPW)MLFMA with four radiation patterns must be employed for $\bar{\mathbf{T}}_{BC}$.

Both this Section on open surfaces and the previous one on closed surfaces deal with frequency ranges that cover most practical applications of electrodynamics. The next Section investigates what happens at extremely low frequencies.

VI. Very Low Frequencies

When using the NSPWMLFMA to accelerate the Calderón preconditioner and the impedance matrix at even lower frequencies, the Calderón preconditioner, as described previously, will eventually break down. In Fig. 9 the condition number of $\bar{\mathbf{T}}_{BC} \cdot \bar{\mathbf{G}}^{-1} \cdot \bar{\mathbf{T}}_{RWG}$ is shown as a function of the frequency, for scattering at a configuration of two small cubes positioned such that they interact through the NSPWMLFMA. It appears that the condition number increases very rapidly from a certain point. A comparison of the three curves for various truncation errors indicates that it is essentially caused by the error introduced by the NSPWMLFMA. Indeed, the explosion of the condition number can be suppressed by increasing L, but obviously this comes with the cost of additional memory and CPU time.

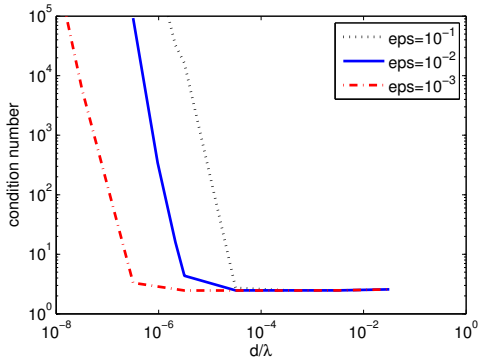

Figure 9. Condition number of $\bar{\mathbf{T}}^2$ as a function of inverse wavelength for various truncation errors.

The instability is caused by cancellation errors, prohibiting $\bar{\mathbf{T}}_{h,BC} \cdot \bar{\mathbf{G}}^{-1} \cdot \bar{\mathbf{T}}_{h,RWG}$ to vanish. For reasons of compactness, in the remainder of this section we will omit the notations BC and RWG, as well as the Gram matrix $\bar{\mathbf{G}}^{-1}$, unless the context requires their presence. As can be derived from (3), with varying frequency, $\bar{\mathbf{T}}_s$ behaves like $\mathcal{O}(k)$ and $\bar{\mathbf{T}}_h$ like $\mathcal{O}\left(\frac{1}{k}\right)$. In Fig. 10 the norm of various constituents of the matrix $\bar{\mathbf{T}}^2$ are displayed as a function of the frequency, for the same two-cube example with a 10^{-2} truncation error. The norm $|\bar{\mathbf{T}}_h \bar{\mathbf{T}}_h|$ is ten orders of magnitude smaller than the product of the norms $|\bar{\mathbf{T}}_h||\bar{\mathbf{T}}_h|$, demonstrating that the cancelling of the hypersingular contribution is very effective. However, no matter how accurate the NSPWMLFMA calculates the distant interactions, there will always be a frequency range where $|\bar{\mathbf{T}}_h \bar{\mathbf{T}}_h| > |\bar{\mathbf{T}}_h \bar{\mathbf{T}}_s|$, destroying the well-behaved properties of the operator.

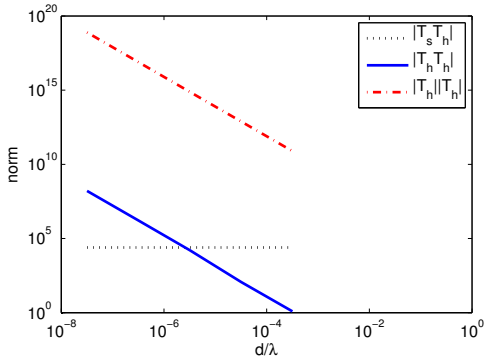

Figure 10. $|\bar{\mathbf{T}}_s \bar{\mathbf{T}}_h|$, $|\bar{\mathbf{T}}_h \bar{\mathbf{T}}_h|$ and $|\bar{\mathbf{T}}_h||\bar{\mathbf{T}}_h|$ as a function of inverse wavelength for truncation error 10^{-2}.

Analysis of the expressions for $\bar{\mathbf{T}}_s$ and $\bar{\mathbf{T}}_h$ in (3) shows that

$$\frac{|\bar{\mathbf{T}}_h \bar{\mathbf{T}}_h|}{|\bar{\mathbf{T}}_s \bar{\mathbf{T}}_h|} \sim \frac{f(\epsilon)}{(kd)^2} \tag{20}$$

with $f(\epsilon)$ a certain function of the accuracy ϵ of the distant interactions, k the wave number and d the typical size of the mesh. An expression for $f(\epsilon)$ is difficult to derive, because it depends on many factors, including box size at the lowest level, n_t and whether or not $L' < L$ (see Section III). As also illustrated by Fig. 9, this means that increasing the accuracy with an order of magnitude delays the instability by the same amount for this small configuration. In general, also for larger objects, Fig. 9 is a good indicator to verify when the instability occurs.

Another problem, related to the previous one but independent of the use of the NSPWMLFMA, limits the achievable accuracy of the iterative process. The term $\bar{\mathbf{T}}_h \cdot \bar{\mathbf{T}}_h \cdot \boldsymbol{X}$ must be negligable, in comparison with $\bar{\mathbf{T}}_h \cdot \bar{\mathbf{T}}_s \cdot \boldsymbol{X}$. Because $\bar{\mathbf{T}}_h$ increases in magnitude with decreasing frequency and the solution of $\bar{\mathbf{G}}^{-1} \cdot \boldsymbol{X}$ is of limited precision ($\approx \kappa_G 10^{-16}$ in double precision, with κ_G the condition number of the Gram matrix), round-off effects in the last significant digit cause the process to eventually stagnate. The number of digits n_i that can be solved for can easily be estimated as

$$n_i = \log_{10} \frac{k^2 d^2}{\kappa_G \epsilon_G}, \tag{21}$$

with $\kappa_G \approx 2$ and $\epsilon_G = 10^{-15}$ the accuracy used to solve $\bar{\mathbf{G}}^{-1} \cdot \boldsymbol{X}$. Figure 11 displays the convergence process (lines) and the estimated limit (21) (circle) for three different frequencies, demonstrating that (21) provides an accurate estimate. It is obvious that a purely multiplicative scheme for the preconditioner can never obtain more accurate digits than a direct inversion, hindered by the condition number of $\bar{\mathbf{T}}_{RWG}$.

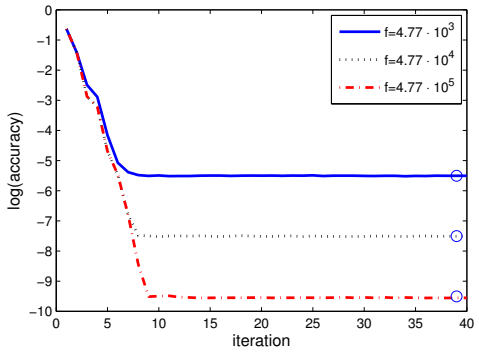

Figure 11. The lines represent the convergence behaviour of the iterative process in the simulation of a small cube, at three different frequencies. The circle indicates the estimated convergence limit, predicted by (21).

Even though usually neither of the above two problems occurs in electrodynamic simulations of practical interest, it is useful to provide a solution. Both can be avoided with the same technique, albeit at a cost of memory and CPU time. Both issues are caused by the failure to cancel $\bar{\mathbf{T}}_h \bar{\mathbf{T}}_h$, hence the only solution is to manually eliminate the term from (8) and give up the strictly multiplicative scheme. A similar approach was used in [5], before the invention of the CMP. In order to save time and memory, the decomposition can be partially recombined as

$$\boldsymbol{T}^2 = (\boldsymbol{T}_h + \boldsymbol{T}_s)\boldsymbol{T}_s + \boldsymbol{T}_s\boldsymbol{T}_h \tag{22}$$

Note that eliminating this term does not introduce a discretisation error (unlike the case of RWG-only schemes [5]), because only numerical errors cause it to be different from zero. There are now two matrix-vector products instead of one. The calculation of $\bar{\mathbf{T}}_{h,RWG} \cdot \boldsymbol{J}$ and $\bar{\mathbf{T}}_{s,RWG} \cdot \boldsymbol{J}$ requires a formulation of the NSPWMLFMA with respectively one and three radiation pattern components. $\bar{\mathbf{T}}_{s,BC} \cdot \boldsymbol{J}$ must also be treated in a scalar way, with three components, while $\bar{\mathbf{T}}_{h,BC} + \bar{\mathbf{T}}_{s,BC}$ requires either four scalar radiation patterns (for open surfaces) or can rely on the vectorial formulation with two components (when the object is closed). The recombination (22) also saves significant memory and time for the near interactions.

Considering the two cube problem at different frequencies treated with the decomposed operators now yields results that are fully stable. When the frequency goes down (experiments went as low as $3.18 \cdot 10^{-7}$ Hz) the condition number and iteration count quickly converge to 2.475 and 11, respectively, when solved for a relative iterative accuracy of 10^{-12}. The omission of $\bar{\mathbf{T}}_h \bar{\mathbf{T}}_h$ makes the formulation unconditionally stable.

VII. Numerical Examples

In this section we will illustrate the capabilities of our approach by means of three examples of increasing electrical size. The first one features metamaterials, which require very fine discretisation. Metamaterials have very fine electric details and are usually only effective at certain resonance frequencies, complicating accurate simulation. In this example we study a material built from small identical spirals (which can be considered as closed PEC objects), leading to macroscopic chirality. To accurately describe the geometrical behaviour, a single spiral requires 4584 unknowns. The discretisation is shown in Fig. 12. A time domain analysis revealed the resonance frequencies of one spiral [24], one of which ($5.98 \cdot 10^6$ Hz) will be used to execute the simulations for a large constellation of spirals as well. A cylinder-shaped metamaterial is constructed using 222 spirals that are oriented identically, shown in Fig. 13, leading to a total of $1\,017\,648$ unknowns. Note that despite the large number of unknowns, the structure itself is small compared to the wavelength, allowing us to use the EFIE alone. For an efficient handling, a parallellised version of the NSPWMLFMA was employed, relying on an asynchronous algorithm [25], which is highly suited for complicated geometries. As explained in [24], the presence of the chiral effect depends on the direction and polarisation of the incoming wave. Two simulations are executed, using the incoming fields schematically represented in Fig. 14. The bistatic radar cross section (RCS) for both is displayed in Fig. 15. In agreement with the predictions, the RCS resulting from the field with oblique incidence displays some asymmetry, while the other one is perfectly symmetrical. In the case of a homogenous and isotropic scatterer, both results would be symmetrical.

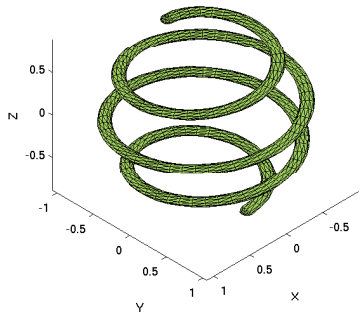

Figure 12. The mesh for one spiral object.

Due to the resonance of the structure, the number of iterations required to get below 10^{-3} accuracy is about 100. Note that these are lossy resonances, which are not related to spurious solutions. If the simulation is repeated at a non-resonant frequency, the number of iterations required becomes as low as 4, but this triggers a much weaker chiral response and is not interesting from an engineering point of view. Due to the very fine mesh, in comparison with the wavelength, these accurate simulations would be nearly impossible without a powerful preconditioner.

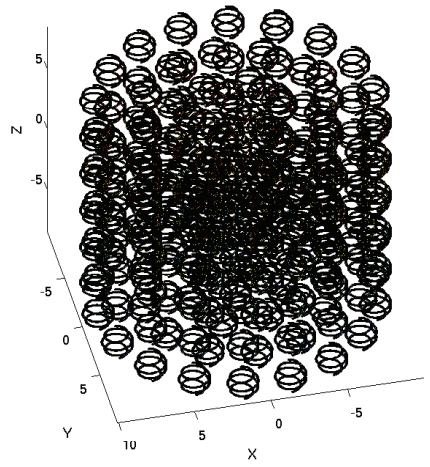

Figure 13. A cylinder-shaped constellation of 222 spiral objects.

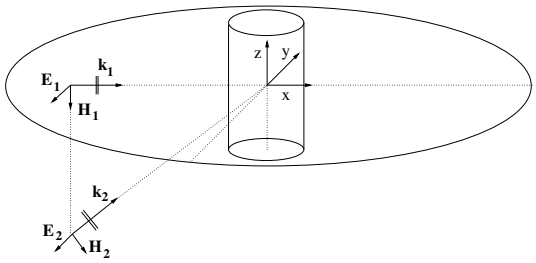

Figure 14. The geometry for the simulation (not to scale), displaying the cylindrical object, the two incoming plane waves and the circle along which the far field is calculated. The first plane wave has $\boldsymbol{k}_1 = (1, 0, 0)$ and $\boldsymbol{E}_1 = (0, -1, 0)$, while the second one is defined by $\boldsymbol{k}_2 = \frac{1}{\sqrt{2}}(1, 0, 1)$ and $\boldsymbol{E}_2 = (0, -1, 0)$.

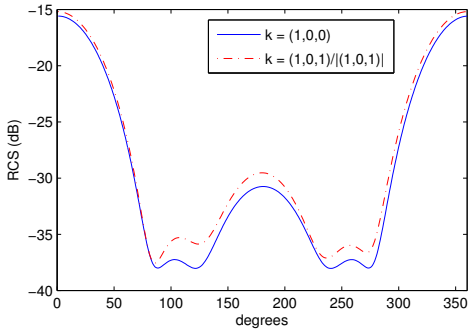

Figure 15. The bistatic RCS (for the Y-component) of the two incoming fields displayed in Fig. 14

In a second example we will demonstrate the performance of the CMP-NSPWMLFMA through the simulation of a geometry featuring many open surfaces, thin objects and sharp corners. In addition, there is a significant amount of non-uniformity present (the ratio of the areas of the largest and smallest triangles present is approximately 50). Figure 16 shows a mesh representing a simplified form of the International Space Station (ISS) as it would look after completion in 2010 (at the time of writing it is approximately 81% finished). As was shown in Section II, the CMP-NSPWMLFMA is particularly useful at low frequencies, and we will study the effect of an incoming left circular polarised plane wave with a wavelength about the size of the ISS. The mesh contains $164\,768$ unknowns. We again employ the EFIE formulation (the closed object is sufficiently small to be below the first resonance). The CMP-NSPWMLFMA algorithm required 121 iterations (for a residual error of 10^{-3}), each iteration requiring 13 seconds. Without preconditioning, a single iteration takes 5 seconds. However, even after 1000 iterations the relative residual error was still close to one. This example, due to its non-uniformity, also demonstrates the need for the diagonal scalers (see Section II). Without the scalers, no significant improvement in the solution is obtained after 1000 iterations. In both this example and the previous one, succesful usage of algebraic preconditioners would be extremely difficult due to the low frequencies (see also Section II). Both examples also required the use of the NSPWMLFMA for an efficient solution, because the lowest level box sizes are much smaller than $\frac{\lambda}{3}$ (which would be about the smallest box size in an MLFMA scheme, see Section III).

In a final example we will look at a structure of multiple wavelengths in size. Figure 17 shows the realistic (open PEC) model of a PC case ($0.21 \times 0.405 \times 0.425\mathrm{m}^3$), as can be used for the calculation of shielding efficiencies. This structure is illuminated by a plane wave ($\lambda = 0.17\mathrm{m}$, $\boldsymbol{k} = (0, -1, 0)$ and $\boldsymbol{E}_{pol} = (0, 1, 0)$). For a normal high frequency problem (discretisation approximately $\frac{\lambda}{10}$), algebraic preconditioners are arguably more performant than the Calderón preconditioner. However, in this case, a fine discretisation was used for very accurate modeling ($\mathrm{d} \approx 0.005\mathrm{m}$) with local refinement near the ventilation holes (see Fig. 17), leading to $200\,127$ unknowns. This relatively dense mesh ($\frac{d}{\lambda} \approx 0.03$) makes the application of sparse algebraic preconditioners undesirable, because the near interaction matrix alone is not sufficient to create an effective preconditioner (see also Section II). In addition, the cavity-like nature of this structure makes preconditioning a necessity. When using a fully dense Calderón preconditioner, the number of iterations (for 10^{-3} relative accuracy on the iterative solution) is 541. When employing a local preconditioner (cutting interactions beyond 1λ) as described in Section V, the number of iterations is reduced to 283, illustrating its effectiveness. Without a preconditioner, the same amount of accuracy is only reached after 6270 iterations. The amplitude of the z-component of the total field is shown in Fig. 18.

VIII. Conclusion

The combination of the NSPWMLFMA and the CMP leads to a very stable and efficient scheme for scattering simulations at PECs. The application, however, is not trivial and the various problems that occur have been explained and solved in the previous sections. Further research will focus on the use of CMP's for dielectric objects as well, as these preconditioners have proven to be very promising in removing the Achilles' heel of surface integral equations in practical applications, namely the lack of guaranteed fast convergence when solved iteratively.

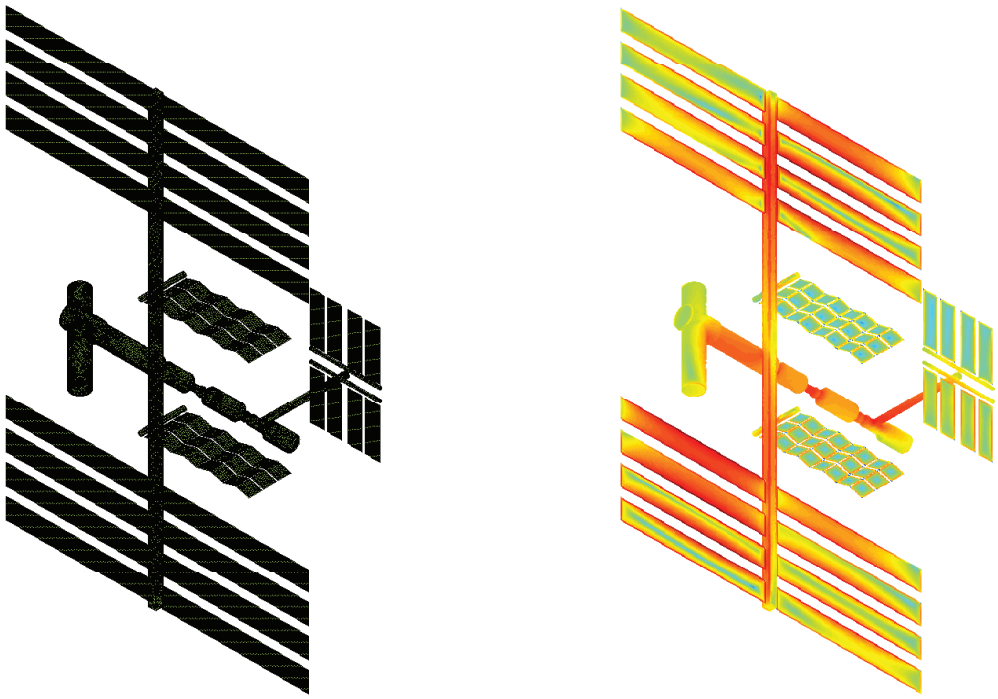

Figure 16. Left: the mesh of the ISS. The habitable parts and the laboratories form one closed object. The solar panels and the two radiatiors (the zigzag structures) are modeled as open surfaces. Each radiator consists of 24 small plates placed closely together. Right: the induced surface current densities as a result from an incoming left circularly polarised plane wave.

REFERENCES

[1] P. Ylä-Oijala, M. Taskinen, and S. Järvenpää, "Analysis of surface integral equations in electromagnetic scattering and radiation problem," *Engineering Analysis with Boundary Elements*, vol. 32, no. 3, pp. 196–209, Mar. 2008.

[2] Ö. Ergül and L. Gürel, "The Use of Curl-Conforming Basis Functions for the Magnetic-Field Integral Equation,," *IEEE Trans. Antennas Propagation*, vol. 54, no. 7, pp. 1917–1926, Jul. 2006.

[3] ——, "Improving the accuracy of the magnetic field integral equation with the linear-linear basis functions,," *Radio Sci.*, vol. 41, Jul. 2006.

[4] S. Borel, D. P. Levadoux, and F. Alouges, "A new well-conditioned integral formulation for Maxwell equations in three dimensions," *IEEE Trans. Antennas Propagation*, vol. 53, no. 9, pp. 2995–3004, Sep. 2005.

[5] R. Adams and N. Champagne, "A numerical implementation of a modified form of the electric field integral equation," *IEEE Trans. Antennas Propagation*, vol. 52, no. 9, pp. 2262–2266, Sep. 2004.

[6] S. M. Rao, D. R. Wilton, and A. W. Glisson, "Electromagnetic scattering by surfaces of arbitrary shape," *IEEE Trans. Antennas Propagation*, vol. AP-30, no. 3, pp. 409–418, May 1982.

[7] A. Buffa and S. H. Christiansen, "A dual finite element complex on the barycentric refinement," *Tech. Report PV-18 IMATI-CNR*, 2005.

[8] W.C. Chew, J. Jin, E. Michielssen, and J. Song, *Fast and Efficient Algorithms in Computational Electromagnetics*. Artech House, 2001.

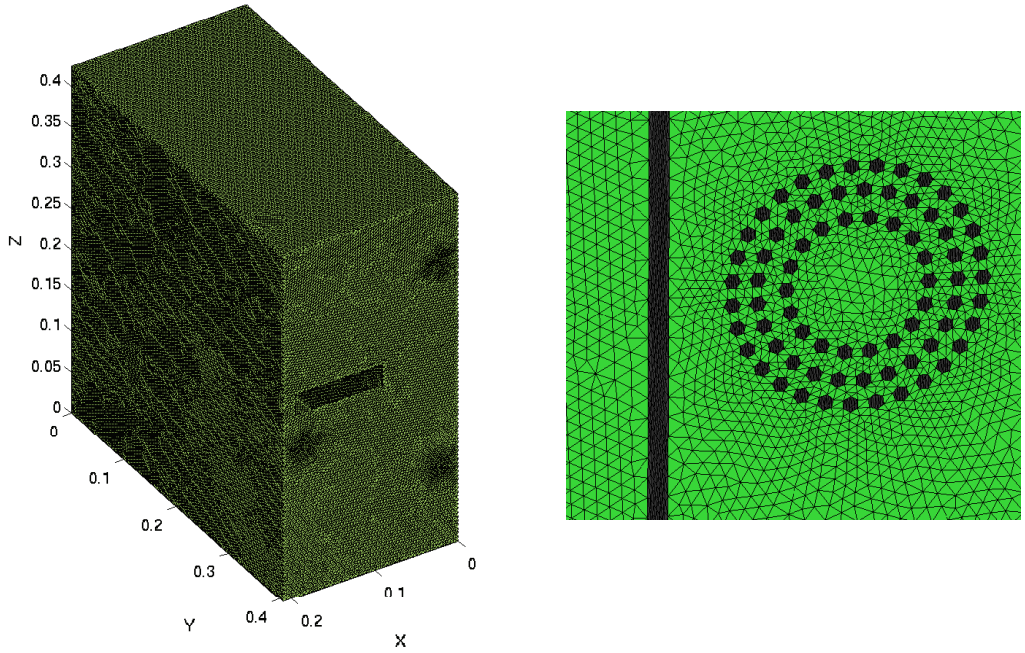

Figure 17. Left: the geometry of the PC case. A slot is shown, through which the field penetrates. The areas of local refinement model small holes. Right: a detail from the backside of the PC case, showing the local refinement around the ventilation holes.

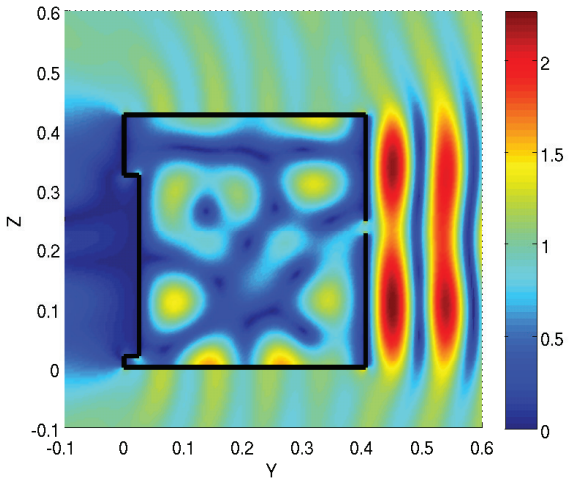

Figure 18. The amplitude of the z-component of the total electric field (V/m) in the YZ-plane, with x=0.1m (see also Fig. 17). The black line indicates the contours of the PC case.

[9] I. Bogaert, J. Peeters, and F. Olyslager, "A nondirective plane wave MLFMA stable at low frequencies," *IEEE Trans. Antennas Propagation*, in press.

[10] H. Wallén and J. Sarvas, "Translation procedures for broadband MLFMA," *Progress In Electromagnetics Research*, no. 55, pp. 47–78, 2005.

[11] I. V. Lindell, *Methods for Electromagnetic Field Analysis*, ser. Oxford Engineering Science Series. Oxford: Clarendon Press, 1992.

[12] R. J. Adams, "Physical and analytical properties of a stabilized electric field integral equation," *IEEE Trans. Antennas Propagation*, vol. 55, pp. 362–372, Feb. 2004.

[13] T. Malas and L. Gürel, "Incomplete LU Preconditioning with the Multilevel Fast Multipole Algorithm for Electromagnetic Scattering," *SIAM J. Sci. Comput.*, vol. 29, no. 4, pp. 1476–1494, Jun. 2007.

[14] T. Malas, Ö. Ergül, and L. Gürel, "Approximate MLFMA as an efficient preconditioner," *Antennas and Propagation Society International Symposium*, pp. 1289–1292, Jun. 2007.

[15] K. Cools, F. Andriulli, F. Olyslager, and E. Michielssen, "Time-domain Calderón identities and their application to the transient analysis of scattering by 3d PEC objects part I: Preconditioning," *IEEE Trans. Antennas Propagation*, submitted.

[16] F. Andriulli, K. Cools, H. Bağci, F. Olyslager, A. Buffa, S. Christiaensen, , and E. Michielssen, "A Multiplicative Calderón Preconditioner for the Electric Field Integral Equation," *IEEE Trans. Antennas Propagation*, vol. 56, no. 8, pp. 2398–2412, Aug. 2008.

[17] H. Bağci, F. Andriulli, K. Cools, F. Olyslager, and E. Michielssen, "A Calderon Multiplicative Preconditioner for the Combined Field Integral Equation," *IEEE Trans. Antennas Propagation*, submitted.

[18] P. Ylä-Oijala and M. Taskinen, "Electromagnetic Scattering Analysis with Combined Field Integral Equations," *Antennas and Propagation International Symposium*, pp. 4869–4872, Jun. 2007.

[19] R. R. Freund, "A transpose-free quasi-minimal residual algorithm for non-hermitian linear systems," *SIAM J. Sci. Comput.*, vol. 14, pp. 137–158, 1993.

[20] J. Sarvas, "Performing interpolation and anterpolation entirely by fast Fourier transform in the 3-D multilevel fast multipole algorithm," *SIAM Journal on Numerical Analysis*, vol. 41, no. 6, pp. 2180–2196, 2003.

[21] I. Bogaert, J. Peeters, and F. Olyslager, "Error control of the vectorial NSPWMLFMA," *IEEE Trans. Antennas Propagation*, in preparation.

[22] P. Ylä-Oijala and M. Taskinen, "Calculation of CFIE Impedance Matrix Elements with RWG and $n\times$ RWG Functions," *IEEE Trans. Antennas Propagation*, vol. 51, no. 8, pp. 1837–1846, Aug. 2003.

[23] W. Schönauer and R. Weiss, "An engineering approach to generalized conjugate gradient methods and beyond," *Applied Numerical Mathematics*, vol. 19, pp. 175–206, 1995.

[24] I. Bogaert, J. Peeters, and F. Olyslager, "Homogenization of metamaterials using full-wave simulations," *Metamaterials*, vol. 2, no. 2–3, pp. 101–112, Sep. 2008.

[25] J. Fostier and F. Olyslager, "An asynchronous parallel MLFMA for scattering at multiple dielectric objects," *IEEE Trans. Antennas Propagation*, vol. 56, no. 9, pp. 2346–2355, Aug. 2008.

IX. Biographies

- Joris Peeters was born on April 16th, 1983. He received the M.S. degree in science and engineering/applied physics in 2006, from Ghent University, Belgium, where he is currently pursuing his Ph.D. Both his interests and research are focused on computational electromagnetism, more in particular the fast and accurate simulation of complicated geometries in broadband frequency ranges.
- Ignace Bogaert was born in Ghent, Belgium, in 1981. He received the M.S. degree in physical engineering from Ghent University, Ghent, Belgium, in 2004. After graduating, he joined the Electromagnetics Group of the Department of Information Technology (INTEC) at Ghent University, where he received his Ph.D in applied physics in 2008. His research is supported by a postdoctoral grant from the Research Foundation-Flanders (FWO-Vlaanderen). His research interests include optimization problems and the modeling of various physical systems, with the emphasis on robustness, efficiency and accuracy.

- Kristof Cools received the B.S degree in mathematics in 2002, M.S. degree in physical engineering in 2004, and the Ph.D. degree in electrical engineering from Ghent University in 2008. His advisors were Prof. Femke Olyslager (Ghent University) and Prof. Eric Michielssen (University of Michigan). Since 2008 he has been a postdoctoral researcher at Ghent University. His research interests are in computational electromagnetics with focus on the spectral properties and discretization schemes of the boundary integral equations encountered in computational electromagnetics. Dr. Cools was the recipient of the Young Scientist Best Paper Award at the 2009 ICEAA Symposium in Torino.
- Femke Olyslager was born in 1966 and died in 2009. She received the Master degree in Electrical Engineering in 1989 and the Ph.D. degree in Electrical Engineering in 1993, both from Ghent University, Ghent, Belgium. She was a Full Professor in electromagnetics at Ghent University. Her research concerned different aspects of theoretical and numerical electromagnetics. She authored or coauthored close to 300 papers in journals and proceedings. She coauthored Electromagnetic and Circuit Modeling of Multiconductor Transmission Lines (Oxford, U.K.: Oxford University Press, 1993) and authored Electromagnetic Waveguides and Transmission Lines (Oxford, U.K.: Oxford University Press, 1999). She was Assistant Secretary General of the International Union of Radio Science (URSI), an Associate Editor of the IEEE TRANSACTIONS ON ANTENNAS AND PROPAGATION and was an Associate Editor of Radio Science. In 1994 she became laureate of the Royal Academy of Sciences, Literature and Fine Arts of Belgium. She received the 1995 IEEE Microwave Prize for the best paper published in the 1993 IEEE TRANSACTIONS ON MICROWAVE THEORY AND TECHNIQUES and the 2000 Best Transactions Paper award for the best paper published in the 1999 IEEE TRANSACTIONS ON ELECTROMAGNETIC COMPATIBILITY. In 2002 she received the Issac Koga Gold Medal at the URSI General Assembly and in 2004 she became laureate of the Royal Flemish Academy of Belgium. She was a Fellow of the IEEE.
- Daniël De De Zutter (M. Sc. 1976, Ph.D. 1981, Habilitation 1984, Ghent University) is now a full professor of Electromagnetics at the Engineering Faculty of Ghent University. In 2000 he was elected to the grade of Fellow of the IEEE. He published more than 160 journal publications. In the period 2004-2008 he served as dean of the faculty. He serves as an associate editor for the IEEE Trans. Microwave Theory and Techniques. At present he is the head of the Department of Information Technology.